


Electric gating and interlayer coupling controllable electronic structure and Schottky contact of graphene/BiI₃ van der Waals heterostructure

Chuong V. Nguyen ^{*}

Department of Materials Science and Engineering, Le Quy Don Technical University, Ha Noi 100000, Viet Nam

 (Received 6 October 2020; revised 9 March 2021; accepted 10 March 2021; published 18 March 2021)

Graphene-based van der Waals heterostructures have received tremendous interest from both fundamental and experimental studies because they can enhance the properties and expand the possibility of applications of both graphene and two-dimensional materials. Motivated by the successful synthesis of the graphene/BiI₃ heterostructure [Chang *et al.*, *Adv. Funct. Mater.* **28**, 1800179 (2018)], here, we systematically investigate the electronic structure and interfacial characteristics of this material using first-principles simulations. We find that the structure of the graphene/BiI₃ heterostructure is mainly characterized by weak van der Waals interactions, which keeps the heterostructure feasible. In the ground state, the graphene/BiI₃ heterostructure forms the *n*-type Schottky contact with a barrier of 0.53 eV. The barriers of the Schottky contact can be adjusted by various factors, including interlayer coupling and electric gating. Both the interlayer coupling and electric gating lead to the transformation from the *n*-type Schottky contact to the *p*-type one or to the *n*-type Ohmic contact. These findings demonstrate that graphene/BiI₃ can be considered a promising building block for high-performance photoresponsive optoelectronic devices.

DOI: [10.1103/PhysRevB.103.115429](https://doi.org/10.1103/PhysRevB.103.115429)

I. INTRODUCTION

Recently, the combination of two or more two-dimensional materials (2DMs) to establish van der Waals (vdW) heterostructures has been proved to be one of the most common strategies to enhance the electronic, optical, and photocatalytic properties of 2DMs, which will strongly affect the performances of 2DMs-based nanodevices [1,2]. Thus, the formation of vdW heterostructures can improve the devices' performances and extend the range of applications of the parent 2DMs. In this way, the formed vdW heterostructures harbor many interesting properties which are absent in the component 2DMs. To date, several vdW heterostructures have been fabricated in experiments and proposed theoretically [3–9]. Generally, vdW heterostructures can be obtained easily in experiments by various methods, including mechanical assembly and direct growth [10–12]. However, the vdW heterostructures can be predicted theoretically by stacking suitable 2DMs on top of others [13–15]. The weak vdW interactions between the 2DMs not only keep the heterostructures energetically stable but also give rise to the simplicity in the exfoliation process. The above-mentioned characteristics demonstrate that the vdW heterostructures have emerged as a promising candidate for a variety of high-performance optoelectronic and nanoelectronic devices [16–21].

Among the 2DM-based vdW heterostructures, graphene-based vdW heterostructures have received tremendous interest from both fundamental and experimental studies because they can enhance the properties and expand the possibility of applications of both graphene and other component 2DMs.

To date, a plethora of experimental strategies have been developed to synthesize graphene-based heterostructures, such as graphene/GaSe [9], graphene/WS₂ [22], graphene/PbI₂ [23], and so forth. Furthermore, a lot of theoretical studies have also been established to explore the physical properties of graphene-based heterostructures as well as their potential applications [24–32]. For instance, Wang *et al.* [32] theoretically predicted that the graphene/GeC heterostructure can yield dynamic switching between the *p*-type and *n*-type Schottky contacts and between a Schottky contact and an Ohmic contact, which indicates that this heterostructure is suitable for high-speed Schottky devices. The formation of the graphene/GeTe heterostructure gives rise to the enhancement of the optical absorption and the extension of potential applications rather than both graphene and GaTe materials [30].

More recently, a new type of 2DM, namely, the *MX*₃ structure (*M* is the metal element, *X* represents the halogen element) was predicted to be a promising candidate for various applications in optoelectronics and nanoelectronics. As an example, bismuth triiodide (BiI₃) has been explored both theoretically and experimentally [33–38]. BiI₃ thin films can be obtained from different techniques, especially van der Waals epitaxy [33]. The electronic structure and photocatalytic performance of the BiI₃ monolayer were theoretically investigated from first-principles simulations [39,40]. This system possesses an indirect band gap semiconductor. In addition, monolayer BiI₃ has been devoted to be dynamically stable; thus, it can be exfoliated from the bulk form. To date, several heterostructures exist through combining the BiI₃ monolayer and other 2DMs, such as BiI₃/WSe₂ [41], BiI₃/silicon [42], and graphene/BiI₃ [43]. Li *et al.* showed that the BiI₃/WSe₂ vdW heterostructure can readily be fabricated and it possesses a distinct photovoltaic effect [41]. The high on-off ratio of

^{*}Corresponding author: chuong.vnguyen@lqdtu.edu.vn

10^9 of BiI₃/silicon [42] makes it suitable for photovoltaic devices. Interestingly, using vdW epitaxy, Chang *et al.* [43] produced a photodetector with ultrahigh responsivity of 6×10^6 A/W based on the graphene/BiI₃ heterostructure. All these findings make the graphene/BiI₃ heterostructure a promising building block for high-performance optoelectronic applications. Motivated by the successful synthesis of the graphene/BiI₃ heterostructure, in this work, we perform first-principles calculations to examine its electronic properties and contact types. Our results could provide theoretical insight into the electronic characteristics of graphene/BiI₃ heterostructure and also helpful information for its use in nanoelectronic and optoelectronic applications.

II. COMPUTATIONAL METHODS

All the simulations and calculations are performed throughout first-principles calculations based on density functional theory (DFT), which is implemented in the QUANTUM ESPRESSO package [44]. The Perdew-Burke-Ernzerhof (PBE) functional of the generalized gradient approximation [45] was selected to perform the exchange-correlation potential. The ion-electron interactions were described by the optimized norm-conserving Vanderbilt pseudopotentials. The simple DFT method fails to understand the weak vdW forces in layered materials; thus, the dispersion-corrected DFT-D3 [46] dispersion approach generated by Grimme was used to correctly describe these forces. The k -point mesh of the Brillouin zone and the cutoff energy of the plane wave are set to be $9 \times 9 \times 1$ and 410 eV, respectively. All the atomic structures of both monolayers and heterostructure are fully relaxed with the convergence of energy and force less than 10^{-6} eV and 0.01 eV/Å, respectively. A large vacuum thickness is set to be 40 Å for all structures, which is enough to avoid the interaction between the periodic layers. Furthermore, the spin-polarized calculations were performed to check for the presence of magnetic behavior. Our spin-polarized calculations showed that the graphene and BiI₃ monolayers as well as their heterostructure exhibit nonmagnetic characteristics at the ground state.

III. RESULTS AND DISCUSSION

Initially, we investigate the structural, electronic, and optical properties of single-layer BiI₃, as illustrated in Fig. 1. We can find from Fig. 1(a) that in the crystal structure of single-layer BiI₃, Bi atoms are sandwiched between two iodine layers. The Bi and I atoms are held together via the strong ionic bonds, whereas the single-layer BiI₃ unit is stacked via weak vdW interactions. The calculated Bi-I bond length and the lattice parameter of the BiI₃ monolayer are 3.12 and 7.62 Å, respectively. These values are in good agreement with previous reports [35], verifying the reliability of our computational approach. Additionally, the band gap of single-layer BiI₃ is 2.58 eV, which is the same as in the previous report [39]. The band structure of single-layer BiI₃ is depicted in Fig. 1(b). The band gap of this material is formed between the valence band maximum (VBM) along the Γ - K path and the conduction band minimum (CBM) at the Γ point. This indicates an indirect band gap semiconductor of single-layer

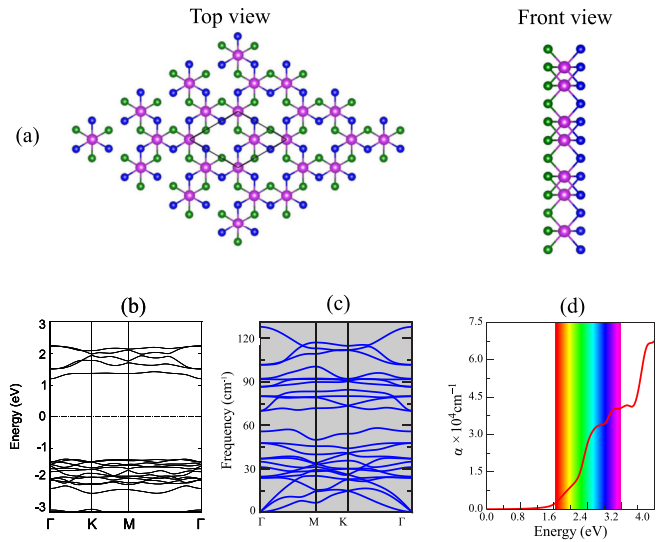


FIG. 1. (a) Top and side views of the atomic structure, (b) band structure, (c) phonon dispersion curves, and (d) optical absorption of single-layer BiI₃. The violet balls represent the Bi atoms, whereas the I atoms in the top and bottom layers of BiI₃ are represented with blue and green balls, respectively.

BiI₃. In addition, it should be noted that Bi is a heavy atom; thus, spin orbit coupling (SOC) is important. However, the presence of the SOC effect leads to only a decrease in the band gap value of the BiI₃ monolayer. The PBE and PBE+SOC methods give quite similar band structures except for the size of the energy gap. Therefore, we used only the PBE approximation to calculate the electronic properties of the considered materials.

The phonon dispersion curves of the BiI₃ monolayer are depicted in Fig. 1(c). The obtained phonon dispersion is in good agreement with available results [36,47], confirming the reliability of our calculations. It can be found that there are no negative phonon branches, indicating that the single-layer BiI₃ structure is mechanically stable and can exist as a freestanding 2D crystal. Furthermore, according to group theory and the symmetry of single-layer BiI₃, the irreducible representation of the phonon modes at the Γ point is given by

$$\Gamma = 4A_g + 4A_u + 4^2E_g + E^2E_u. \quad (1)$$

The calculated optical absorption of monolayer BiI₃ in Fig. 1(d) shows that it can effectively adsorb the visible light, indicating its high potential for photovoltaic applications.

We now construct the atomic structure of the graphene/BiI₃ heterostructure by stacking graphene on top of the BiI₃ monolayer. Based on the quantitative relation of the lattice parameters of monolayer graphene (~ 2.46 Å) and monolayer BiI₃, we build the graphene/BiI₃ heterostructure using a supercell comprising a $(3 \times 3 \times 1)$ graphene supercell and a $(1 \times 1 \times 1)$ BiI₃ supercell. The lattice parameter of the graphene/BiI₃ heterostructure is 7.50 Å, which is the average of the lattice parameters of the graphene and BiI₃ supercells. This gives rise to a small lattice mismatch of only 1.6% in the graphene/BiI₃ heterostructure. According to previous experiments and theoretical calculations, when the strain is as high as 20%, the single-layer graphene

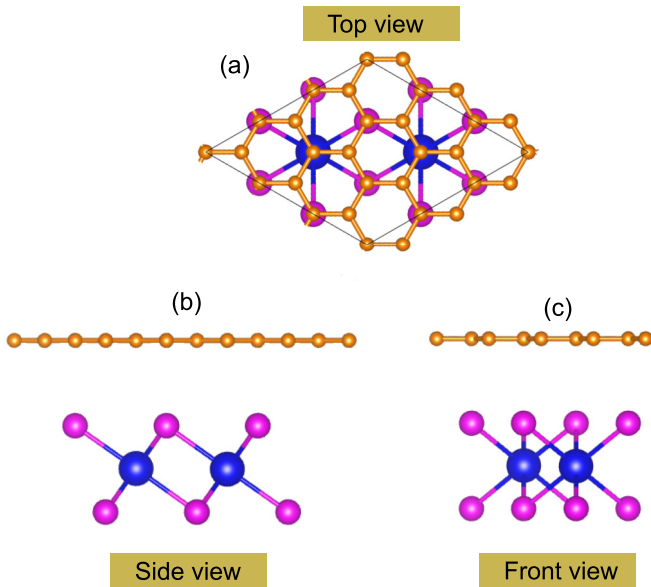


FIG. 2. (a) Top view, (b) side view, and (c) front view of the graphene/ BiI_3 heterostructure.

can still maintain the semimetallic characteristics of the Dirac cones [48–50]. The relaxed atomic structure of the graphene/ BiI_3 heterostructure is depicted in Fig. 2. In this stacking configuration, C atoms are placed on top of B and I atoms. After geometric optimization, the interlayer distance between the graphene and iodine layer of BiI_3 is 3.55 Å. Interestingly, this distance is the same as that reported in other graphene-based vdW heterostructures [30,51], but it is still larger than the buffer-substrate distance between buffer carbon and interfacial $\text{SiC}(0001)$ [52], where the buffer carbon is pinned to the SiC substrate due to a strong sp^3 covalent bonding. Furthermore, the interlayer spacing is related to the bonding situation at the interface. When the interface exhibits covalently bonding or partially covalent interactions, the interlayer spacing is generally less than 3 Å, while the interfacial vdW interaction usually results in an interlayer spacing of 3–4 Å [52–54]. These findings suggest the physical bonding between graphene and BiI_3 rather than the chemical bonds. Furthermore, to clarify the bond nature in graphene/ BiI_3 , we next calculate its binding energy as follows:

$$E_b = \frac{E_H - E_G - E_B}{N_C}. \quad (2)$$

Here, the total energies of graphene/ BiI_3 , isolated graphene, and BiI_3 monolayers are defined by E_H , E_G , and E_B , respectively. N_C is 18, which represents the total number of C atoms in the calculated supercell. From Eq. (2), we obtain the binding energy per C atoms in the graphene/ BiI_3 heterostructure, which is calculated to be -34.86 meV/C atom. The negative sign in the binding energy indicates that the graphene/ BiI_3 heterostructure is energetically stable. In addition, we find that such a value for the binding energy is close to that in other graphene heterostructures [30,51]. This finding suggests that the graphene/ BiI_3 heterostructure is characterized mainly by

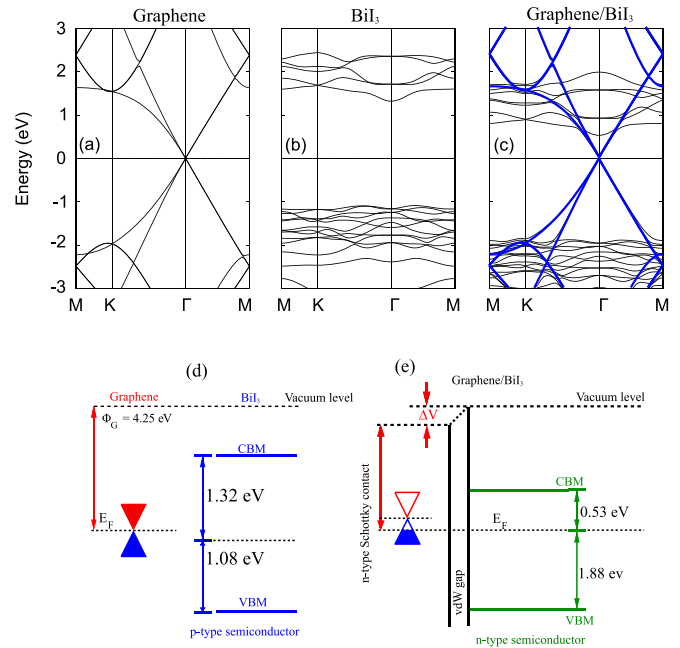


FIG. 3. Calculated band structures of (a) the isolated graphene supercell, (b) BiI_3 , and (c) the graphene/ BiI_3 heterostructure. The blue lines represent the contributions of graphene layer in the graphene/ BiI_3 heterostructure. The band diagram of graphene and BiI_3 (d) before and (e) after the formation of the heterostructure.

weak vdW interaction, making the graphene/ BiI_3 heterostructure feasible.

The electronic band structure of the graphene/ BiI_3 heterostructure as well as the isolated graphene and BiI_3 supercells is illustrated in Fig. 3. We can find from the projected band structure of the graphene/ BiI_3 heterostructure as illustrated in Fig. 3(c) that no gap states are formed within the band gap of the BiI_3 layer, denoting that the Fermi level pinning is absent in the graphene/ BiI_3 Schottky contact. The absence of Fermi level pinning was also in other graphene-based vdW heterostructures, such as graphene/transition metal dichalcogenides [55,56]. Graphene possesses a semimetallic character with a linear dispersion cone around the Fermi level, as depicted in Fig. 3(a). Interestingly, the Dirac point is shifted from the K point in perfect graphene to the Γ point in the graphene supercell owing to the band-folding effect [28,57]. However, the BiI_3 monolayer shows a semiconducting nature with an indirect band gap, as illustrated in Fig. 3(b). The band gap of the BiI_3 supercell is calculated to be 2.40 eV, which is slightly smaller than that of a perfect BiI_3 monolayer. The indirect band gap nature in the BiI_3 supercell remains as in the perfect one. In addition, the isolated BiI_3 monolayer exhibits a p -type semiconductor, as in Fig. 3(d). The electronic band structures of the graphene/ BiI_3 heterostructure are depicted in Fig. 3(c). Several interesting features exist when the graphene/ BiI_3 heterostructure is formed. First, the band structures of this heterostructure seem to be a combination of those of both graphene and BiI_3 layers. This gives rise to the preservation of intrinsic electronic properties of graphene and BiI_3 monolayers in their heterostructure. Second, the weak interactions in this heterostructure give rise to the formation

of a small band gap in graphene. The band gap opened in graphene around the Fermi level is calculated to be 17.2 meV, which is smaller than the thermal fluctuation at room temperature (26 meV). It should be noted that a similar band gap opened in graphene was also observed in our previous graphene-based heterostructures [7,24]. It should be noted that in the graphene/BiI₃ heterostructure, the vdW interaction between graphene and the BiI₃ substrate induces out-of-plane deformations in graphene which results in a strain field and, consequently, in a pseudomagnetic field. On the other hand, the different electronegativities of C, Bi, and I atoms also lead to a nonuniform attractive force distribution over graphene. Nonuniform strain in graphene results in a pseudomagnetic field and, consequently, results in the opening of an energy gap. The gap indicates that when putting graphene on monolayer BiI₃, the nonuniform potential breaks the inversion symmetry and induces a band gap. Moreover, the strong SOC in the BiI₃ monolayer has a significant influence on the graphene Dirac states that may result in the topologically nontrivial band structure, which is confirmed by the calculated nontrivial Z_2 index and an explicit demonstration of metallic edge states. However, in this work, from the first-principles calculations based on density functional theory, we identified the most energetically favorable arrangement from all the considered structures where electronic states close to the Fermi energy are dominated by the p_z orbitals of carbon atoms. The interplay between sublattice symmetry breaking determines the size and topological nature of the gaps in the system [58,59]. When the gaps are dominated by the sublattice symmetry breaking, the system becomes a valley Hall insulator [60,61]. We hope that this interesting issue will be investigated in a future study. Furthermore, the formation of the graphene/BiI₃ heterostructure leads to a shift in the Fermi level of BiI₃ toward a higher binding energy. This indicates that the BiI₃ monolayer is switched from a p -type semiconductor to an n -type one. The nature of such switching can be explained by the charge transfer between graphene and the BiI₃ monolayer in their heterostructure. It is clear from Fig. 4 that the charge depletion regions around graphene layer demonstrate electron outflow. However, the charge accumulation regions located near the BiI₃ layer signify electron inflow to the BiI₃ layer. This finding indicates that the graphene layer donates electrons to the BiI₃ layer and introduces shallow donor states close to the conduction band edge, resulting in n -type doping of the BiI₃ monolayer.

It is crucial to mention that when the graphene/BiI₃ heterostructure is formed, it results in the formation of the metal-semiconductor contact, including the Schottky or Ohmic contact. Depending on the position of the Fermi level relative to the VBM and CBM of the semiconducting BiI₃ monolayer, we find that the graphene/BiI₃ heterostructure forms the Schottky contact type (SCT). According to the Schottky-Mott rule [62], the n -type and p -type SCTs can be obtained on the basis of the relative alignment of energy levels, as depicted in Fig. 3(e) as follows:

$$\Phi_n = E_{\text{CBM}} - E_F, \quad (3)$$

$$\Phi_p = E_F - E_{\text{VBM}}. \quad (4)$$

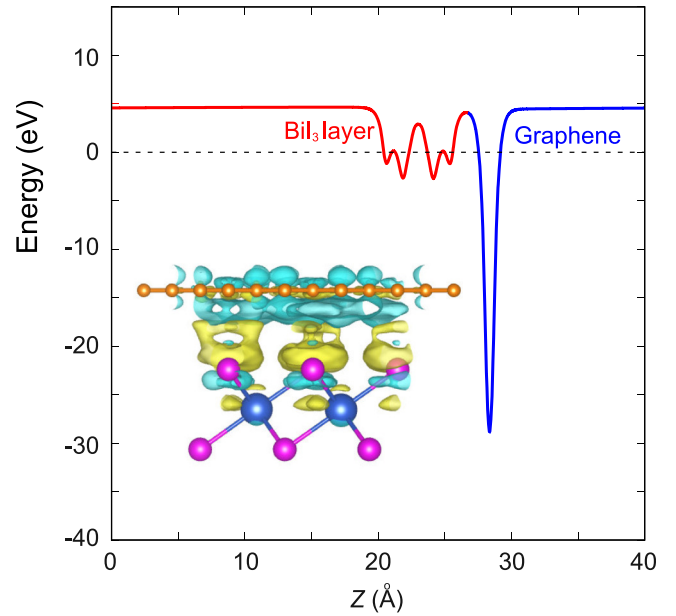


FIG. 4. The calculated electrostatic potential along the z direction of the graphene/BiI₃ heterostructure. The inset is the charge density difference, with the charge accumulation and depletion represented by yellow and cyan regions, respectively.

Here, Φ_n and Φ_p represent the n -type and p -type SCTs of the heterostructure. E_{CBM} , E_{VBM} , and E_F stand for the energy positions of the CBM, VBM, and Fermi level. The calculated Φ_n and Φ_p of the heterostructure are 0.53 and 1.88 eV, respectively, implying that such a heterostructure forms an n -type SCT with a barrier of 0.53 eV.

Furthermore, we establish the charge density difference (CDD) and the electrostatic potential of the graphene/BiI₃ heterostructure. All these calculations are illustrated in Fig. 4. The CDD in the graphene/BiI₃ heterostructure is depicted in the inset. The CDD in this heterostructure is obtained from the difference in the charge densities of the heterostructure (ρ_H) and the constituent monolayers (ρ_M), that is,

$$\Delta\rho = \rho_H - \sum\rho_M. \quad (5)$$

From Eq. (5), we find that the negative charges are mainly visualized around the graphene layer, whereas the I layer has positive charges. This finding implies that the charges are mainly accumulated in the I layer, whereas they are depleted in the graphene layer of the graphene/BiI₃ heterostructure. The electrons are transferred from the graphene to the BiI₃ layers. This transfer gives rise to the electron-holes separation at the interface. In addition, our Bader charge analysis shows that there is only 0.025 electron, which is transferred between graphene and BiI₃ layers in the graphene/BiI₃ heterostructure. The work function of monolayers and their heterostructure is also calculated to explain the charge redistribution at the interface. The work function of the BiI₃ layer is still larger than that of graphene, implying that the BiI₃ layer acquires electrons from graphene. Moreover, the potential of graphene is lower than that of the BiI₃ layer, as presented in Fig. 4, leading to formation of a strong built-in electric field across the interface. This demonstrates that graphene can be used

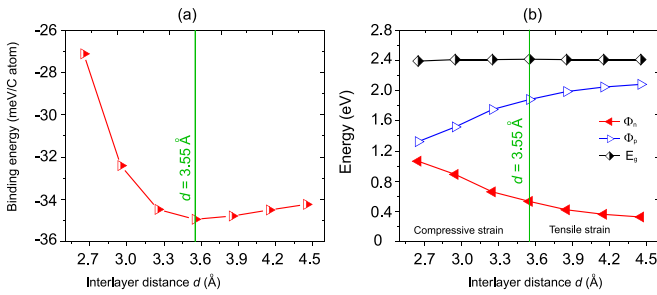


FIG. 5. (a) Binding energy and (b) Schottky barriers of the graphene/ BiI_3 heterostructure as a function of interlayer distances.

as an electrode to achieve electron injection, where electrons would flow from graphene to the BiI_3 channel through the contacted BiI_3 region.

It is clear that electrons flow from graphene to the BiI_3 monolayer, resulting in the formation of an interface dipole [63] that can be defined via a potential step ΔV at the interface, as depicted in Figs. 3(d) and 3(e). The potential step can be defined as $\Delta V = \Phi_{\text{Graphene}/\text{BiI}_3} - \Phi_{\text{Graphene}}$, where $\Phi_{\text{Graphene}/\text{BiI}_3}$ and Φ_{Graphene} are the work functions of the graphene/ BiI_3 and isolated graphene monolayers, respectively. The calculated potential step in the graphene/ BiI_3 heterostructure is 0.37 eV, indicating that the formation of the graphene/ BiI_3 heterostructure causes the Fermi level of BiI_3 to shift upward to a higher binding energy.

Interestingly, the performances of high-speed components are mostly affected by the electronic properties of materials. Therefore, it is necessary to check the controllable electronic properties of combined heterostructure under several external conditions, including interlayer coupling and external electric gating. The effect of interlayer coupling is examined by modifying the interlayer distance between graphene and BiI_3 layers. The compressive strain is obtained by decreasing the interlayer distance, whereas the tensile strain leads to an increase in the interlayer distance. The external electric gating is applied along the z direction of the heterostructure. The direction of electric gating, pointing from graphene to the BiI_3 layer, represents the positive direction.

The variation of the binding energy and the barriers of SCT of the graphene/ BiI_3 heterostructure as a function of interlayer distances is illustrated in Fig. 5. The binding energy of this heterostructure increases with increasing or decreasing the interlayer distances. It indicates that the binding energy at the equilibrium interlayer distance of 3.55 Å is lowest, as depicted in Fig. 5(a). The variation of the Schottky barriers of the graphene/ BiI_3 heterostructure in Fig. 5(b) shows that Φ_n decreases with increasing d , whereas Φ_p increases. It indicates that the switch from n -type to p -type SCT can be achieved in the graphene/ BiI_3 heterostructure. Figure 5(b) indicates the transformation from n -type to p -type SCT under the compressive strain by decreasing the interlayer distance down to 2.6 Å. On the other hand, with increasing the interlayer distance, Φ_n continuously decreases, whereas Φ_p increases. This change may also predict that with continuous stretching of the interlayer distance larger than 5.2 Å, Φ_n continues to approach to the zero level, further leading to an Ohmic contact (OCT) at the interface. The zero or negative

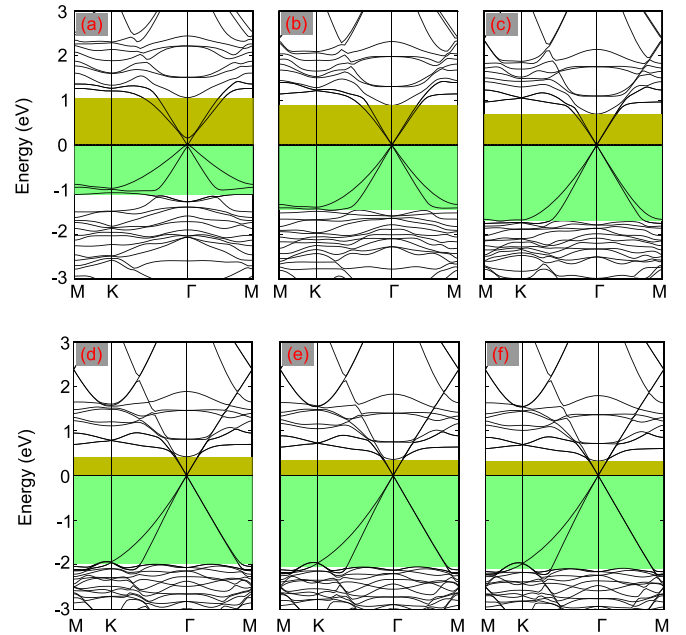


FIG. 6. Calculated band structures of the graphene/ BiI_3 heterostructure under different interlayer spacings of (a) 2.65, (b) 2.95, (c) 3.25, (d) 3.85, (e) 4.15, and (f) 4.45 Å.

value of the barrier of the SCT demonstrates the transformation from the SCT to the OCT. The changing nature of the barriers of the SCT in the graphene/ BiI_3 heterostructure can be explained by analyzing its band structures with different interlayer spacings. These band structures are depicted in Fig. 6. With the reduction of the interlayer spacings from the equilibrium state $d = 3.55$ Å to 2.65 Å, the interlayer coupling between graphene and BiI_3 layers is enhanced. Thus, it gives rise to the shift of the Fermi energy level to the lower binding energy. Indeed, from the band structures of the graphene/ BiI_3 heterostructure, we find that the Fermi level moves downwards from the CBM to the VBM of the semiconducting BiI_3 layer with increasing compressive strain. This shift tends to a decrease in Φ_p and an increase in Φ_n . When the interlayer distance is smaller than 2.6 Å, Φ_p continuously decreases and becomes smaller than Φ_n , implying the switch from the n -type SCT to the p -type one. By increasing the interlayer distance from the equilibrium state up to 4.45 Å, as depicted in Figs. 6(d) and 6(e), the Fermi level moves towards the higher binding energy from the VBM up to the CBM of the semiconducting BiI_3 material. This implies that with increasing interlayer distance Φ_p increases and Φ_n decreases. The Fermi level of the heterostructure moves towards the higher binding energy from the VBM to the CBM of the semiconducting BiI_3 material. The Fermi level is continuously moved towards the CBM with increasing interlayer distance, and it can cross the CBM, resulting in the transition from SCT to OCT in the graphene/ BiI_3 heterostructure. Therefore, we can conclude that the interlayer coupling can switch the n -type SCT into the p -type one and convert the n -type SCT into the OCT in the graphene/ BiI_3 heterostructure. Furthermore, when the interlayer coupling is changed, it also results in an increase (decrease) in the band gap value (opening in graphene).

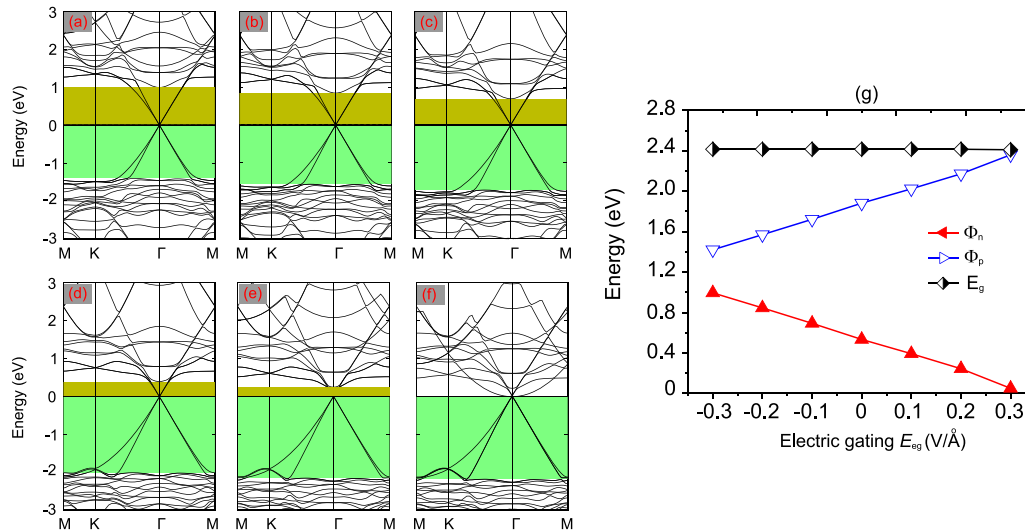


FIG. 7. Calculated band structures of the graphene/BiI₃ heterostructure under different strengths of electric gating: (a) -0.3 , (b) -0.2 , (c) -0.1 , (d) $+0.1$, (e) $+0.2$, and (f) $+0.3$ V/Å. (g) The evolution of the barriers of SCT as a function of electric gating.

Next, we examine the effect of electric gating on the electronic properties of the graphene/BiI₃ heterostructure. The electric gating is applied perpendicularly to the heterostructure surface in the range from -0.3 to $+0.3$ V/Å. In our case, we assume that the graphene/BiI₃ heterostructure is placed inside the capacitor, from which the electric field is generated. The electric field is penetrated through the whole graphene layer. The electric field outside and inside the graphene/BiI₃ is the same when the out-of-plane dielectric polarization is calculated to be zero. Thus, there will be no surface charge on either graphene or the BiI₃ layer. A strength of the applied electric gating of 0.6 V/Å has been realized in experiments by using pulsed ac field technology [64]. The changes in the band structures and the barriers of the SCT in the graphene/BiI₃ heterostructure are illustrated in Fig. 7. Similar to the interlayer coupling, the electric gating is also considered a key factor to modulate the electronic characteristics of the heterostructure. With the presence of the negative electric gating, the Fermi level of this heterostructure is shifted from the CBM towards the VBM of the semiconducting BiI₃ layer, as depicted in Figs. 7(a)–7(c). This finding leads to an increase in Φ_n and a decrease in Φ_p . However, with the application of the positive electric gating, the Fermi level moves from the VBM towards the CBM of the semiconducting BiI₃ layer, as illustrated in Figs. 7(d)–7(f). In this case, Φ_p increases, while Φ_n increases accordingly. The evolution of the barriers of the SCT of the graphene/BiI₃ heterostructure as a function of electric gating is presented in Fig. 7(g). We find that both the barriers of the SCT present the linear dependence as a function of electric gating. This implies that Φ_n can reach approximately zero at the critical electric gating of 0.3 V/Å. In this case, the Fermi level crosses the CBM of the semiconducting BiI₃ material, as presented in Fig. 7(f). Interestingly, it should be noted that due to a linear behavior in the change in the barriers of the SCT, Φ_p will be smaller than Φ_n , indicating a transformation from the n -type SCT to the p -type one. However, achieving this transformation requires applying a large electric gating of

-0.43 V/Å, which cannot be achieved in current experiments. Therefore, applying the electric gating can only adjust the switch of the graphene/BiI₃ heterostructure from the n -type SCT to the n -type OCT, making this heterostructure suitable for potential applications for Schottky devices.

IV. CONCLUSIONS

In summary, we have performed first-principles calculations to examine the electronic behavior and contact types of a vdW heterostructure by combining graphene and the novel BiI₃ material. The results indicate that this heterostructure is energetically stable and characterized by weak vdW forces, which keep the heterostructure feasible at room temperature. At the ground state of an interlayer distance of 3.55 Å, the graphene/BiI₃ heterostructure forms the n -type Schottky contact with a barrier of 0.53 eV. The work function of the BiI₃ layer is still larger than that of graphene, implying that the BiI₃ layer acquires electrons from graphene and electrons would flow from graphene to the BiI₃ channel through the contacted BiI₃ region. Furthermore, we considered the effects of interlayer coupling and electric gating on the electronic properties and contact types of heterostructure. Our results demonstrated that the barriers of the Schottky contact can be adjusted the interlayer coupling and electric gating. Both the interlayer coupling and electric gating resulted in the transformation from the n -type Schottky contact to the p -type one or to the n -type Ohmic contact. Our results could provide theoretical insight into the electronic characteristics of the graphene/BiI₃ heterostructure and provide helpful information for its use in nanoelectronic and optoelectronic applications.

ACKNOWLEDGMENTS

This research is funded by the Vietnam National Foundation for Science and Technology Development (NAFOSTED) under Grant No. 103.01-2019.05.

- [1] S.-J. Liang, B. Cheng, X. Cui, and F. Miao, *Adv. Mater.* **32**, 1903800 (2020).
- [2] W. Liao, Y. Huang, H. Wang, and H. Zhang, *Appl. Mater. Today* **16**, 435 (2019).
- [3] F. Han, Z. Song, M. H. Nawaz, M. Dai, D. Han, L. Han, Y. Fan, J. Xu, D. Han, and L. Niu, *Anal. Chem.* **91**, 10657 (2019).
- [4] S. Wang, C. Ren, H. Tian, J. Yu, and M. Sun, *Phys. Chem. Chem. Phys.* **20**, 13394 (2018).
- [5] F. Ceballos, M. Z. Bellus, H.-Y. Chiu, and H. Zhao, *ACS Nano* **8**, 12717 (2014).
- [6] Y. Chen, X. Wang, G. Wu, Z. Wang, H. Fang, T. Lin, S. Sun, H. Shen, W. Hu, J. Wang, J. Sun, X. Meng, and J. Chu, *Small* **14**, 1703293 (2018).
- [7] H. T. T. Nguyen, M. M. Obeid, A. Bafekry, M. Idrees, T. V. Vu, H. V. Phuc, N. N. Hieu, L. T. Hoa, B. Amin, and C. V. Nguyen, *Phys. Rev. B* **102**, 075414 (2020).
- [8] Z. Ben Aziza, D. Pierucci, H. Henck, M. G. Silly, C. David, M. Yoon, F. Sirotti, K. Xiao, M. Eddrief, J.-C. Girard, and A. Ouerghi, *Phys. Rev. B* **96**, 035407 (2017).
- [9] Z. Ben Aziza, H. Henck, D. Pierucci, M. G. Silly, E. Lhuillier, G. Patriarche, F. Sirotti, M. Eddrief, and A. Ouerghi, *ACS Nano* **10**, 9679 (2016).
- [10] C. R. Dean, A. F. Young, I. Meric, C. Lee, L. Wang, S. Sorgenfrei, K. Watanabe, T. Taniguchi, P. Kim, K. L. Shepard, and J. Hone, *Nat. Nanotechnol.* **5**, 722 (2010).
- [11] T. Yang, B. Zheng, Z. Wang, T. Xu, C. Pan, J. Zou, X. Zhang, Z. Qi, H. Liu, Y. Feng, W. Hu, F. Miao, L. Sun, X. Duan, and A. Pan, *Nat. Commun.* **8**, 1906 (2017).
- [12] X. Li, M.-W. Lin, J. Lin, B. Huang, A. A. Puretzky, C. Ma, K. Wang, W. Zhou, S. T. Pantelides, M. Chi, I. Kravchenko, J. Fowlkes, C. M. Rouleau, D. B. Geohegan, and K. Xiao, *Sci. Adv.* **2**, e1501882 (2016).
- [13] M. Sun, J.-P. Chou, J. Yu, and W. Tang, *Phys. Chem. Chem. Phys.* **19**, 17324 (2017).
- [14] W. Zhang, D. Chang, Q. Gao, C. Niu, C. Li, F. Wang, X. Huang, C. Xia, and Y. Jia, *J. Mater. Chem. C* **6**, 10256 (2018).
- [15] S. Wang, H. Tian, C. Ren, J. Yu, and M. Sun, *Sci. Rep.* **8**, 12009 (2018).
- [16] T. Roy, M. Tosun, M. Hettick, G. H. Ahn, C. Hu, and A. Javey, *Appl. Phys. Lett.* **108**, 083111 (2016).
- [17] L. Britnell, R. Gorbachev, R. Jalil, B. Belle, F. Schedin, A. Mishchenko, T. Georgiou, M. Katsnelson, L. Eaves, S. Morozov, N. Peres, J. Leist, A. Geim, K. Novoselov, and L. Ponomarenko, *Science* **335**, 947 (2012).
- [18] P.-H. Shih, T.-N. Do, G. Gumbs, and M.-F. Lin, *Phys. E (Amsterdam, Neth.)* **118**, 113894 (2020).
- [19] P.-H. Shih, T.-N. Do, B.-L. Huang, G. Gumbs, D. Huang, and M.-F. Lin, *Carbon* **144**, 608 (2019).
- [20] S. Cao, Y. Xing, J. Han, X. Luo, W. Lv, W. Lv, B. Zhang, and Z. Zeng, *Nanoscale* **10**, 16805 (2018).
- [21] L. Ye, H. Li, Z. Chen, and J. Xu, *ACS Photonics* **3**, 692 (2016).
- [22] H. Henck, Z. Ben Aziza, D. Pierucci, F. Laourine, F. Reale, P. Palczynski, J. Chaste, M. G. Silly, F. Bertran, P. Le Fevre, E. Lhuillier, T. Wakamura, C. Mattevi, J. E. Rault, M. Calandra, and A. Ouerghi, *Phys. Rev. B* **97**, 155421 (2018).
- [23] S. Sinha, T. Zhu, A. France-Lanord, Y. Sheng, J. C. Grossman, K. Porfyrakis, and J. H. Warner, *Nat. Commun.* **11**, 823 (2020).
- [24] C. V. Nguyen, M. Idrees, H. V. Phuc, N. N. Hieu, N. T. T. Binh, B. Amin, and T. V. Vu, *Phys. Rev. B* **101**, 235419 (2020).
- [25] P.-H. Shih, T.-N. Do, G. Gumbs, H. D. Pham, and M.-F. Lin, *Opt. Lett.* **44**, 4721 (2019).
- [26] K. D. Pham, N. N. Hieu, H. V. Phuc, I. Fedorov, C. Duque, B. Amin, and C. V. Nguyen, *Appl. Phys. Lett.* **113**, 171605 (2018).
- [27] L. Cao, Y. S. Ang, Q. Wu, and L. Ang, *Appl. Phys. Lett.* **115**, 241601 (2019).
- [28] Y. Li, J. Wang, B. Zhou, F. Wang, Y. Miao, J. Wei, B. Zhang, and K. Zhang, *Phys. Chem. Chem. Phys.* **20**, 24109 (2018).
- [29] Y. Zhang, X. He, M. Sun, J. Wang, and P. Ghosez, *Nanoscale* **12**, 5067 (2020).
- [30] X. Gao, Y. Shen, Y. Ma, S. Wu, and Z. Zhou, *Comput. Mater. Sci.* **170**, 109200 (2019).
- [31] A. Bafekry, M. M. Obeid, C. V. Nguyen, M. Ghergherehchi, and M. Bagheri Tagani, *J. Mater. Chem. A* **8**, 13248 (2020).
- [32] S. Wang, J.-P. Chou, C. Ren, H. Tian, J. Yu, C. Sun, Y. Xu, and M. Sun, *Sci. Rep.* **9**, 5208 (2019).
- [33] S. Takeyama, K. Watanabe, M. Ichihara, K. Suzuki, and N. Miura, *J. Appl. Phys.* **68**, 2735 (1990).
- [34] N. J. Podraza, W. Qiu, B. B. Hinojosa, H. Xu, M. A. Motyka, S. R. Phillpot, J. E. Baciaik, S. Trolier-McKinstry, and J. C. Nino, *J. Appl. Phys.* **114**, 033110 (2013).
- [35] C. Shen and G. Wang, *J. Mater. Sci.* **52**, 11513 (2017).
- [36] F. Ma, M. Zhou, Y. Jiao, G. Gao, Y. Gu, A. Bilic, Z. Chen, and A. Du, *Sci. Rep.* **5**, 17558 (2015).
- [37] A. J. Lehner, H. Wang, D. H. Fabini, C. D. Liman, C.-A. Hébert, E. E. Perry, M. Wang, G. C. Bazan, M. L. Chabinyk, and R. Seshadri, *Appl. Phys. Lett.* **107**, 131109 (2015).
- [38] R. E. Brandt, R. C. Kurchin, R. L. Hoyer, J. R. Poindexter, M. W. Wilson, S. Sulekar, F. Lenahan, P. X. Yen, V. Stevanovic, J. C. Nino, M. G. Bawendi, and T. Buonassisi, *J. Phys. Chem. Lett.* **6**, 4297 (2015).
- [39] H. Yan, H. Ziyu, G. Xu, and S. Xiaohong, *Chem. Phys. Lett.* **691**, 341 (2018).
- [40] P. Liu, F. Lu, M. Wu, X. Luo, Y. Cheng, X.-W. Wang, W. Wang, W.-H. Wang, H. Liu, and K. Cho, *J. Mater. Chem. C* **5**, 9066 (2017).
- [41] J. Li, X. Guan, C. Wang, H.-C. Cheng, R. Ai, K. Yao, P. Chen, Z. Zhang, X. Duan, and X. Duan, *Small* **13**, 1701034 (2017).
- [42] C.-S. Li, S.-W. Kuo, Y.-T. Wu, P.-H. Chang, I.-C. Ni, M.-H. Chen, and C.-I. Wu, *Adv. Mater. Interfaces* **7**, 2000630 (2020).
- [43] P.-H. Chang, C.-S. Li, F.-Y. Fu, K.-Y. Huang, A.-S. Chou, and C.-I. Wu, *Adv. Funct. Mater.* **28**, 1800179 (2018).
- [44] P. Giannozzi *et al.*, *J. Phys.: Condens. Matter* **21**, 395502 (2009).
- [45] J. P. Perdew, K. Burke, and M. Ernzerhof, *Phys. Rev. Lett.* **80**, 891 (1998).
- [46] S. Grimme, S. Ehrlich, and L. Goerigk, *J. Comput. Chem.* **32**, 1456 (2011).
- [47] W.-B. Zhang, L.-J. Xiang, and H.-B. Li, *J. Mater. Chem. A* **4**, 19086 (2016).
- [48] F. Liu, P. Ming, and J. Li, *Phys. Rev. B* **76**, 064120 (2007).
- [49] C. Lee, X. Wei, J. W. Kysar, and J. Hone, *Science* **321**, 385 (2008).
- [50] V. M. Pereira, A. H. Castro Neto, and N. M. R. Peres, *Phys. Rev. B* **80**, 045401 (2009).
- [51] D. P. de Andrade Deus and I. S. S. de Oliveira, *J. Phys.: Condens. Matter* **32**, 355501 (2020).

- [52] M. Conrad, J. Rault, Y. Utsumi, Y. Garreau, A. Vlad, A. Coati, J.-P. Rueff, P. F. Miceli, and E. H. Conrad, *Phys. Rev. B* **96**, 195304 (2017).
- [53] H. Guo, Z. Zhang, Y. Guo, Z. Gao, R. Zheng, and H. Wu, *Appl. Surf. Sci.* **505**, 144650 (2020).
- [54] S. Li, M. Sun, J.-P. Chou, J. Wei, H. Xing, and A. Hu, *Phys. Chem. Chem. Phys.* **20**, 24726 (2018).
- [55] T. Le Quang, V. Cherkez, K. Nogajewski, M. Potemski, M. T. Dau, M. Jamet, P. Mallet, and J. Veuillen, *2D Mater.* **4**, 035019 (2017).
- [56] Y. Liu, P. Stradins, and S.-H. Wei, *Sci. Adv.* **2**, e1600069 (2016).
- [57] Y.-C. Zhou, H.-L. Zhang, and W.-Q. Deng, *Nanotechnology* **24**, 225705 (2013).
- [58] A. M. Alsharari, M. M. Asmar, and S. E. Ulloa, *Phys. Rev. B* **94**, 241106(R) (2016).
- [59] Z. Wang, D.-K. Ki, H. Chen, H. Berger, A. H. MacDonald, and A. F. Morpurgo, *Nat. Commun.* **6**, 8339 (2015).
- [60] A. M. Alsharari, M. M. Asmar, and S. E. Ulloa, *Phys. Rev. B* **97**, 241104(R) (2018).
- [61] M. Gmitra, D. Kochan, P. Högl, and J. Fabian, *Phys. Rev. B* **93**, 155104 (2016).
- [62] R. T. Tung, *Appl. Phys. Rev.* **1**, 011304 (2014).
- [63] A. Di Bartolomeo, *Phys. Rep.* **606**, 1 (2016).
- [64] C. Vicario, B. Monoszlai, and C. P. Hauri, *Phys. Rev. Lett.* **112**, 213901 (2014).